ELECTE DEC 1 9 1988

H

20. DISTRIBUTION/AVAILABILITY OF ABSTRACT  X☐ UNCLASSIFIED/UNLIMITED X☐ SAME AS RPT. ☐ DTIC USERS	21. ABSTRACT SECURITY CLASSIFICAT UNCLASSIFIED	TION 44
22a. NAME OF RESPONSIBLE INDIVIDUAL R J BARKER	22b. TELEPHONE (Include Area Code) (202) 767-5011	22c. OFFICE SYMBOL AFOSR/NP

### FINAL REPORT

### ON THE RESEARCH GRANT

AFOSR-84-0041

## NUMERICAL MODELING OF NARROW BAND SOFT X-RAY SOURCES

For the Period

Approved for public release; distribution unlimited.

15 Nov 1983 - 14 Aug 1987

## Submitted to

Dr Robert J. Barker
Air Force Office of Scientific Research
AFOSR/NP, Building 410
Bolling Air Force Base
Washington, DC 20332

by

Richard L. Morse, Professor Dept of Nuclear Engineering and Dept of Physics University of Arizona Tucson, Arizona 85721 Chief, Fachy Later Chemiation Division

TOP 15 Constitute TO DITIO en and the class open reviewed and is and constitute less that AFR 190-12.

FFECE OF COMMITTED FESEARCH (AFSO)

# TABLE OF CONTENTS

		Page
	LIST OF ILLUSTRATIONS	•
	ABSTRACT	vii
1.	INTRODUCTION	1
2.	THE HYDRODYNAMICS	10
3.	THE RADIATION TRANSFER	13
4.	THE GEOMETRY	19
5.	RESULTS	22
6.	CONCLUSIONS	62
	APPENDIX A: VARIOUS DERIVATIONS	63
	APPENDIX B: CONTRIBUTION OF THE CONTINUUM	. 72
	REFERENCES	75

OUALITY	INSPECTED 2	
Acces	sion Fo	ř
DTIC Unann	GRARI TAB ounced fication	
By	ibution	
	labilit	
	Avail 6	ind/or
Dist	Speci	.al
PY		

# LIST OF ILLUSTRATIONS

Figure	Page
1. Angles in Spherical Geometry	7
2. Procedure Flow Chart	9
3A. Impact Parameter Groups	15
3B. Impact Parameter Groups as Seen By One Point	16
3C. Transport Scheme	18
4. Impact Parameter Group Boundaries	21
5. Laser Pulse Shape	23
6. Target Model	26
7. Laser Energy Deposition	28
8A. Electronic Temperature	30
8B. Electronic Temperature	31
9A. Ionic Temperature	32
9B. Ionic Temperature	33
10A. Aluminum Density	34
10B. Aluminum Density	35
10C. Aluminum Density	36
11. Expansion Velocity	37
12A. Electronic and Ionic Densities	39
12B. Electronic and Ionic Densities	40
13. Total Output Power	42
14. Total Output Energy	43
15. Time-integrated Emission Spectrum	44

## LIST OF ILLUSTRATIONS -- Continued

Figure		Page
16.	Time-integrated Heg Line	46
17A.	Time-integrated H <sub>Q</sub> Doublet Two-Level Approximation	47
17B.	Time-integrated H <sub>Q</sub> Doublet Multi-level Treatment	48
18.	Time-integrated Heg Line	49
19.	Time-integrated H <sub>β</sub> Line	50
20.	Time-resolved Emission Spectrum at Peak Power	51
21.	Time-resolved He at Peak Power	52
22A.	Time-resolved H Doublet at Peak Power Two-level Approximation	53
22B.	Time-resolved H <sub>a</sub> Doublet at Peak Power Multi-level Treatment	54
23.	Time-resolved He Line at Peak Power	55
24.	Time-resolved HB Line at Peak Power	56
25A.	Ha Doublet with No Doppler Shift	57
25B.	Ha Doublet with 25% of Doppler Shift	58
25C.	Ha Doublet with 50% of Doppler Shift	59
25D.	Ha Doublet with 75% of Doppler Shift	60

#### ABSTRACT

A model has been developed for calculating x-ray line emission from spherical plasmas.

The main features of this method are:

- 1) Plasma parameters are obtained from a one-dimensional Lagrangian hydrodynamics and heat flow code.
- 2) Multi-frequency groups: the line structure can be reproduced with the desired accuracy by adjusting the number of frequency groups.
- 3) Self consistent, time dependent excited level populations and radiation fluxes: the code starts with coronal populations, calculates the ensuing radiation flux and then recalculates the populations and so on, iterating until convergence is reached.
- 4) Geometrical groups of rays grouped by spherical impact parameter.
- 5) Line broadening due to ionic thermal agitation and Doppler shift due to the net plasma flow velocity. Inclusion of the flow velocity shift would be difficult without the multi-frequency group treatment.

The method has been applied to an aluminum target, and the results are in good agreement with previous experimental work. The total energy, summed over all lines, as well as the line intensity ratios (which are a sensitive measure of agreement with experiment) were predicted with good accuracy. The pictures that would be seen by a pinhole camera are also calculated by the code.

#### INTRODUCTION

The scope of this work is to calculate the transport in and emission of x-rays from a spherical plasma created by laser-heating of a spherical target.

The setting for such experiments is as follows: a spherical target is hit from every direction by a laser pulse split into a number of beams so as to approximate spherical symmetry. Due to the intense energy deposition, part of the material is instantly vaporized and ionized, thereby creating a plasma cloud of density decreasing with radius. As is known, light of frequency f cannot penetrate a plasma of electronic density equal to or greater than a 'critical density' at which the plasma frequency equals the frequency of the incoming light. The radius at which the electronic density in the spherical target plasma equals the critical density for the frequency of the laser light defines the 'critical surface.' Energy is transported inward of the critical surface mainly by electronic thermal conduction. The intrinsic non-linearity of the heat transfer in plasmas produces a thermal front propagating inward: the thermal wave. The temperature distribution has therefore two opposite faces: from the thermal front out the high conductivity of the electrons makes the spatial behavior of the

temperature very smooth, whereas inward of the thermal front the temperature drops abruptly and the plasma is essentially cold.

the hot part of the plasma is a very strong x-ray emitter, and the present work has as goal to predict what an observer looking at the plasma from outside would see.

This task is two-fold: modeling the hydrodynamics of the process and modeling the x-ray transfer. The first is modeled by a hydrodynamics and heat flow code discussed later on. This code outputs its results at discrete time steps. A post-processor code models the transport of radiation through the plasma.

The time scale of atomic processes is very short compared to the time step of the hydrocode. We can therefore take the view that the atomic processes are essentially instantaneous, or, to put it another way, that the atomic quantities are essentially in steady state.

In this view, as every new hydrocode time step is taken, ionization and excitation processes take place instantly and the ionic species densities and excited level populations so produced remain then unchanged until next time step.

The transport of radiation through a plasma and the ensuing emission of light have been investigated many times and by many authors, and several different approximations have been made at different times.

Particularly, a point that does not seem to have received overwhelming attention is the feedback effect that the radiation field intensity has on the excited state populations and, thereby, on the various parameters characterizing the transport (i.e. emissivity and

absorptivity). The problem here is that the population of the excited levels determines the light intensity, and the light intensity plays a role in determining the population of the excited levels. A one-step, exact solution of the problem is therefore extremely difficult in the simplest cases and impossible generally.

In fact, much work has been done assigning some guessed instantaneous limiting form of equilibrium to the populations then calculating the radiation transport and emission sustained by such populations. The criteria proposed for the guesswork have been several, each one appropriate to a particular range of conditions. Three in particular have come up more frequently: LTE, Coronal equilibrium and Escape factors.

The first two imply some guess as to what the radiation intensity will eventually be, approaching black body in the first case and approaching zero in the second. The third, the Escape factors method, is a more sophisticated procedure, first developed by Holstein [1,2] who actually solved the self-consistent problem. This last method, unlike the other two, takes into account the effect of the actual radiation field on the excited state population. In it, one first calculates the coronal population, then the optical depth of the plasma in the center of the line with such population, and from the depth a coefficient, greater than one, by which to multiply the coronal value to obtain the population of the excited levels.

But in fact the problem can be exactly solved only with an iterative procedure in which an initial guess on either the population

or the light intensity is followed by repeated calculations of both to follow their mutual relaxation until some convergence criterion is met.

To accomplish this, it is necessary to know the emission and absorption profiles. As is well known, atoms do not emit sharp, delta-function-like lines. Several phenomena combine to distribute the emission (and the absorption) over a profile of some width. The three main such phenomena are natural, Stark, and Doppler broadening. The natural line width is estimated from

 $\Delta E \cdot \Delta t \sim \hbar$  where  $\Delta t \sim 1/A_{21}$  $\Delta E \sim \hbar \cdot A_{21} \sim 10^{-2} \text{ eV}$ .

As for the Stark broadening [8,6]:

 $\Delta E \sim 8.8 \ 10^{-16} \ \Omega_{12} \ n_e \ eV$ 

 $\Omega_{12} n_e < 10^{12} s^{-1}$  for  $He_a$  line in A1, therefore

 $\Delta E < 10^{-3} \text{ eV}$ .

The Doppler broadening is significantly greater than either of the above. Furthermore, an effect that has not received much attention in previous work is the frequency shift due to the expansion velocity of the plasma. Neglecting it can be acceptable in dealing with astrophysical sources, but is clearly inadequate for the laboratory sources of x-ray, in which we are primarily interested, since sizeable plasma flow velocities, in units of local sound speed, can be reached. It is a general property of ablative flows to generate velocities from zero to supersonic, and the difference in velocity of different parts of

the plasma is such that the difference in Doppler shift can be of the same order of the local Doppler width. This entails that parts of the plasma that would be optically thick at rest, become transparent to radiation from other parts of the plasma because of their motion. We have, therefore, used a multi-frequency group numerical method that makes it possible to include Doppler shift from flow in these calculations. A Doppler profile of width dependent on the local ionic temperature is assumed in the present work, for both emission and absorption profiles, assumed identical.

Since the code transports one energy group at a time, it is convenient to take a somewhat backward point of view: instead of modifying the fequency of the incoming ray to the frame of the flowing plasma, we shift the absorption-emission profile of the moving plasma, as it is seen in the lab frame. Since the flow velocity varies with the radius, the Doppler shift changes through any given shell. It is therefore necessary to define a line shape that is an average throughout the shell (see Appendix A for the derivation of this average).

Finally, we have dealt with the angular distribution of the intensity with a novel perspective: in spherical symmetry the direction is generally described in local spherical polar coordinates in which the polar axis is, at every point in space, the radius through that point. Due to the evident azimuthal symmetry, only the colatitude needs to be taken into account, and the parameter most widely used is the cosine of the colatitude, that is, the cosine of the angle that, at the given point, the direction considered makes with the radius; this cosine is

generally, and will be throughout this work, indicated with  $\mu$  (see Figure 1).

What is generally done in numerical transport schemes is discretize  $\mu$  into 'angular groups.' Instead of introducing angular groups, we follow a number of rays, each one representative of a group of rays and characterized by its distance of closest approach to the center of the sphere (its 'impact parameter') in its path through the plasma. Those are the groups of characteristics in spherical geometry. By using them, we eliminate some diffusion truncation error that would be introduced by the use of angle groups.

Summarizing, the novelty of our approach to the radiation transfer resides in three points which we will call self-consistency, Doppler effect and impact parameter groups. We shall now proceed to discuss the numerical algorithm developed to model this physical situation.

To outline the procedure briefly (See Figure 2):

- The atomic properties of the material are read in. The laser and target parameters are read by the hydrocode. A hydrocode run is made separately.
- 2) The hydrocode output is read, at the current time step, in a post-processing mode. Cold zones are recognized.
- 3) Ionic species densities and electronic density in every 'hot' zone are calculated.
- 4) The transition rates are computed. The population is initialized as coronal.

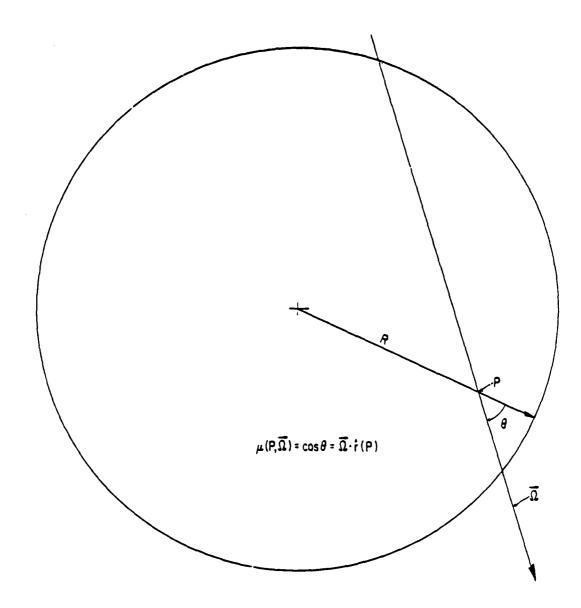


Figure 1: Angles in Spherical Geometry

- 5) Iteration is started: radiation flux is computed and then fed into the rate equation to obtain the next iterate for the population, then the radiation flux is recalculated and so on until convergence is reached.
- 6) Back to point 2) for the next hydrocode time step.

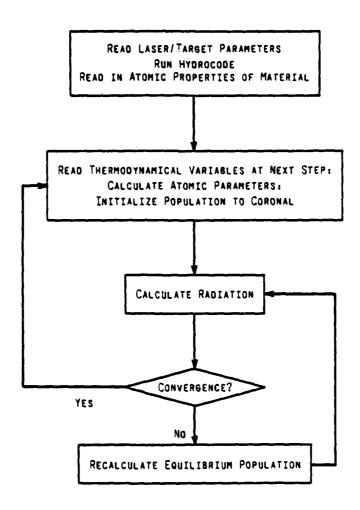


Figure 2: Procedure Flow Chart

### THE HYDRODYNAMICS

The hydrodynamics is modeled by Chamisa, a code developed by R. Malone to model the implosion of targets and used by K. Matzen and R. Morse to model ablative flows. The code follows the expansion of the plasma in time due to the laser energy deposition.

The sphere is divided into n shells, or zones, around a cold central ball. The thermodynamical quantities are assumed constant throughout any given shell.

The code outputs at discrete time steps:

Outer radius  $r_k$  and thickness  $\Delta r_k$  Electronic and ionic temperatures  $Te_k$  and  $Ti_k$  Ionic density  $Ni_k$  and expansion velocity  $vx_k$  this for every zone k.

This output is read by the transfer code.

A zone which does not meet given requirements on electronic temperature and ionic density is labeled 'too cold' and considered inactive. This leaves n' 'active' zones. For every active zone the densities of the various ionic species and the electronic density are calculated using the ionization and recombination coefficients calculated by Summers [4,5]. In the treatment of the excitation states we will assume that ionization and recombination play a negligible role

in swapping electrons from a level to another, and we will neglect it.

In this way, determining the ionic composition of the plasma and calculating the excitation states are two totally decoupled problems.

In the first round of calculations, we used the less demanding (in terms of computing time and memory requirements) "Two-level atom' approximation. This well known simplifying hypothesis consists in assuming the atom capable of being in one of only two states: the ground level and the (single) excited level (henceforth referred to, respectively, as levels 1 and 2). This assumption essentially means transporting one line at a time, implying that the radiation field due to transitions between one pair of levels does not influence the population equilibrium of other pairs. Of course, this assumption is better suited to situations in which the frequencies of the transitions are very far apart and, also, the ground state populations is essentially unchanged by the excitation state.

We found, as expected, that it is not quite adequate to treat lines that are close enough to each other. Furthermore, we are interested in treating, as the next application of this code, x-ray lasing, which requires considering transitions between several excited levels. We have therefore generalized the code to treat multiple levels.

In the following, we shall refer to the lower and upper level of any one transition as levels 1 and 2.

The information on electronic and ionic densities is used to calculate collisional excitation and deexcitation coefficients ( $\Omega_{12}$  and

 $\Omega_{2,1}$ ) [6] which, together with Einstein's coefficients (A<sub>2,1</sub>, B<sub>1,2</sub> and B<sub>2,1</sub>), determine the rate equations for the atomic transitions between an excited level and the ground state.

(II-1) 
$$\frac{dn_{2}}{dt} = (\Omega_{12} \ n_{e} + B_{12} \int_{0}^{\infty} \phi \ E^{J} E^{dE}) \ n_{1}$$
$$- (A_{21} + \Omega_{21} \ n_{e} + B_{21} \int_{0}^{\infty} \phi \ E^{J} E^{dE}) n_{2}$$

where  $\phi_E$  is the line profile,  $J_E$  is the direction-averaged light intensity and  $n_i$  are the appropriate densities.

The results reported here are found considering only transfer of resonant lines, though the code can treat transitions between excited levels. Initial runs including the continuum support the results of experiments being conducted, e.g. by H. Epstein [7], and show that the contribution of the continuum is of negligible importance. The excited population is obtained by assuming steady state (i.e. equating the right side of (II-1) to zero). This means assuming the characteristic time scale of the hydrodynamic processes to be much longer than the time scale of atomic transitions, although the code could easily treat time dependence of level populations on the hydro time scale.

<sup>\*</sup> See Appendix B

### THE RADIATION TRANSFER

The more conventional transport schemes working in spherical geometry, generally devised to describe neutron transport, might seem very apt to model the transfer of light, once one sees the light as a collection or beam of photon, i.e., neutral particles only interacting at close contact with scattering centers, and in this respect very much like neutrons. What such schemes generally do is discretize the interval  $-1 \le \mu \le 1$  (where  $\mu$  is the cosine of the angle that the direction considered makes with the radius.) into a number of angle groups, which is a natural choice in planar geometry. But in curved geometries, a straight trajectory (such as an unscattered neutron or photon) can belong to different angle groups at different radii. Therefore, in such geometries, an angular group treatment requires shifting particles from one group to another when need arises due to the change in spatial coordinate, with resulting numerical diffusion. A very classical example could be the Sn approximation. But taking the view of geometric optics, which is how we generally look at light, it seemed more appropriate to do the contrary, that is, adjust the groups to the radial position in such a way that a ray (which is straight in the absence of significant refraction) remains in the angular group throughout the transport.

Having chosen this approach, it seems a natural choice to characterize the groups of rays by their 'impact parameter', that is,

the distance of closest approach of the rays representative of the groups to the center of the sphere. This procedure has the fringe benefit of readily yielding the intensity as a function of radius in the projection of the spherical image on a plane. That is, the emitting sphere as seen by a pin-hole camera.

As for the choice of the groups, which is to say of the impact parameter of the characteristics, it is determined largely by the hydrodynamics description used. Because our plasma is modeled as a number of concentric spherical shells, it is natural to assign an impact parameter to every shell. Our choice has been to take as impact parameter group boundaries the inner and outer radius of all active shells,\* and as impact parameter of the representative ray the average between them. This leads to two possible situations, as illustrated by Figures (3 A and B): every ray crosses its 'critical' zone, that is, the zone whose inner and outer radii encompass the impact parameter of the ray, in a way much different from the way it crosses all the remaining zones external to the critical one. It is therefore necessary to specify together with the 'normal' transport algorithm, its limiting form for the special case of the critical zone.

As for the boundary conditions, they stem from the requirement of continuity of the flux at every boundary between zones.

<sup>\*</sup> Extra impact parameters through the cold inner plasma can be added at will for better resolution near the axis.

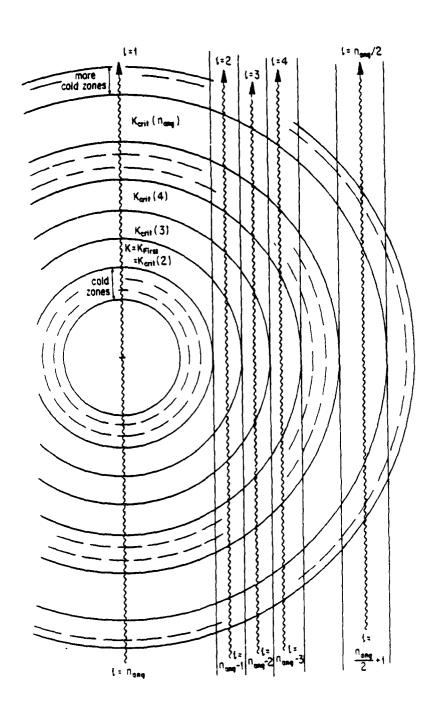


Figure 3A: Impact Parameter Groups

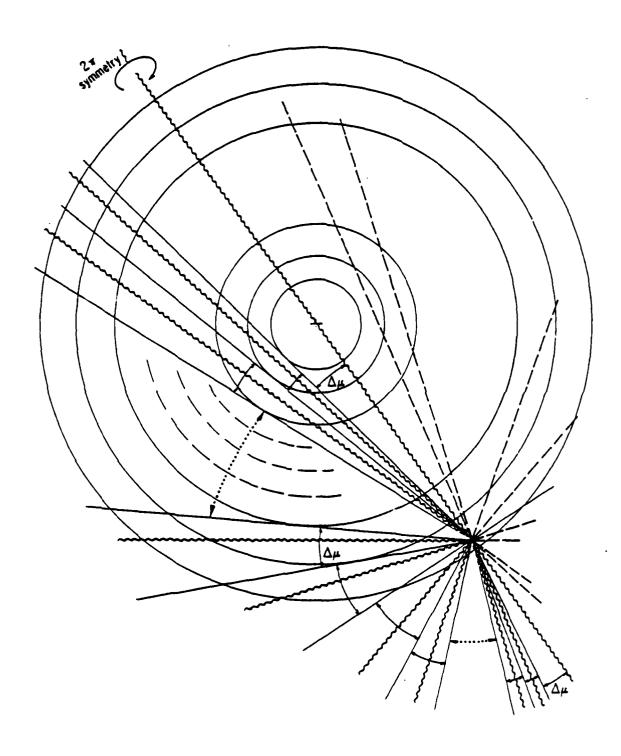


Figure 3B: Impact Parameter Groups as Seen by One Point

Particularly, the ingoing flux at the outermost surface is nul.

A somewhat less obvious condition on the innermost surface is that the flux from inside the surface toward the inside of the first shell is nul.

So, if we follow a 'line of sight', or ray (see Figure 3C), we start with zero intensity at the external surface and build up intensity proceeding inward through the 'normal' zones, then through the 'critical' zone in which the direction changes from inward to outward, then again (but this time proceeding outward) through all the normal zones and finally get the output at the outermost surface.

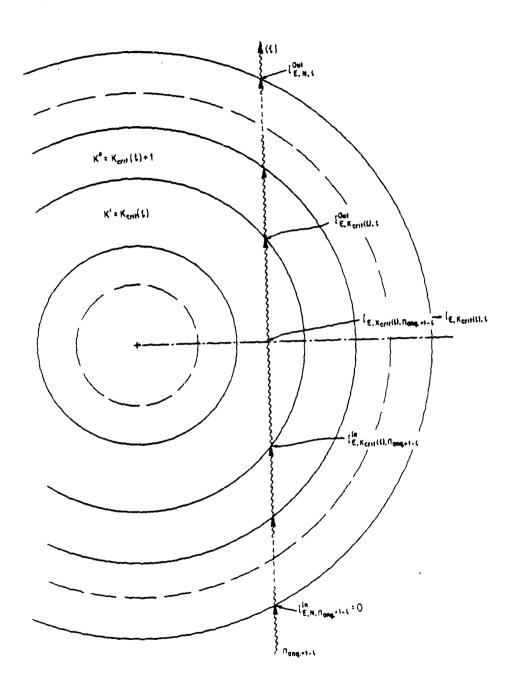


Figure 3C: Transport Scheme

#### THE GEOMETRY

Let us examine the geometry in detail. We have  $n'=n-n_{cold}$  zones, and we set n'+1 impact parameters, that is, through the n' active zones and through the origin.

For every group  $\ell$ , a critical zone remains defined with zone number  $k_{crit}(\ell)$  such that  $r(k_{crit}(\ell)-1) < dist(\ell) < r(k_{crit}(\ell))$ , where  $dist(\ell)$  is the impact parameter of the  $\ell$ th line of sight. For purpose of computation we will consider  $n_{ang}=2(n'+1)$  angular groups, that is, for every ray we consider two groups: outward  $(\ell)$  and inward  $(n_{ang}-\ell+1)$ , so that a group turns into its opposite crossing the critical zone.

A  $\mu_{\mathbf{k},\ell}$  is therefore defined as the cosine of the angle between the  $\ell'$ th ray and the radius at the surface k. An angular span  $2\pi\Delta\mu_{\mathbf{k},\ell}$  is associated with every  $\mu_{\mathbf{k},\ell}$ , such that

$$(IV-1) \qquad \sum_{\ell} \Delta \mu_{k,\ell} = 2.0 \qquad \forall k$$

The exact prescription may vary, as long as (IV-1) is satisfied. Our choice has been as follows.

For every group  $\ell$ , let us define two more directions, one with impact parameter  $r(k_{\text{crit}}(\ell)-1)$  and one with impact parameter  $r(k_{\text{crit}}(\ell))$ , that is to say, one tangent to the inner surface of the

critical zone (for the  $\ell$ th group) and one tangent to its outer surface. Call those lines  $\ell^{<}$  and  $\ell^{>}$ . (See Figure 4).

Evidently, dist( $\ell$ ) < dist( $\ell$ ). Such rays, in the very same way as ray  $\ell$ , define cosines  $\mu_{k,\ell}$  and  $\mu_{k,\ell}$  for every zone k and group 1.

We define Augl as

(IV-2) 
$$\Delta \mu_{\mathbf{k},\ell} = \mu_{\mathbf{k},\ell}^{>} - \mu_{\mathbf{k},\ell}^{<} \qquad \forall \mathbf{k},\ell$$

It is apparent that  $\mu$  and  $\Delta\mu$  change through a given zone, for any given ray. It shall be necessary to define an average  $\Delta\mu_{\mathbf{k},\ell}$ , to be used in the finite difference equation. Again the main requirement is that  $\Delta\mu_{\mathbf{k},\ell}$  obey (IV-1). For the sake of simplicity we have set  $\Delta\mu_{\mathbf{k},\ell}=\Delta\mu_{\mathbf{k},\ell}$ , that is, the average in the shell equal to the value on the outer boundary. This choice can be justified as follows: for any ray  $\ell$  in the critical zone the external surface serves both as entrance and exit surface. In all other zones the change in span  $\Delta\mu$  through the zone is limited.

We are going to use the following notations for intensities:

in 
$$I_{E,k,\ell} = I_E(R_{in,k},\ell)$$

$$\widetilde{I}_{E,k,\ell} = \text{average of } I_{E}(r,\ell) \text{ in } [r_{k-1},r_k]$$

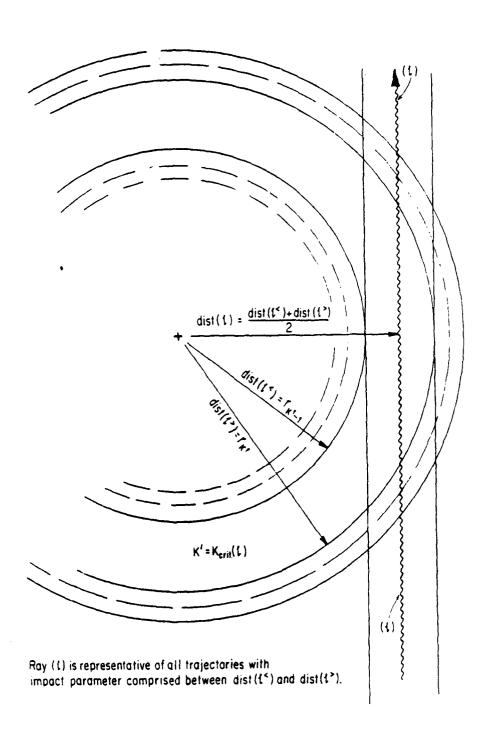


Figure 4: Impact Parameter Group Boundaries

#### RESULTS

In recent years there has been an increasing interest in intense beams of soft x-rays for various applications. Very bright x-ray sources are needed, for instance, for the purpose of etching semiconductors now that a reduction in size of one or two orders of magnitude is sought, and the commonly used ultraviolet beams lack the resolution needed for such miniaturization. Laser produced plasmas are a prime source of such x-rays, due to their very intense brightness and high conversion efficiency.

One apparatus to produce such x-ray beams consists of a powerful Nd-glass laser whose beam is directed against an aluminum flat target[7]. The ensuing short-lived plasma emits very strongly in the 1-2 KeV region of the spectrum. A high repetition rate makes up for the short life of the plasma. The actual target consists of an aluminum cylinder that rotates and advances, not unlike in an old phonograph, and the laser beam is focused on a 40 µm spot. About 10 pulses per second are shot at the cylinder surface, which meanwhile rotates and translates so as to offer a fresh target to every pulse. Each laser shot is actually composed of two gaussian pulses (see Figure 5), a preheating pulse 10 ns long and depositing 1.5J of ene-gy, followed,

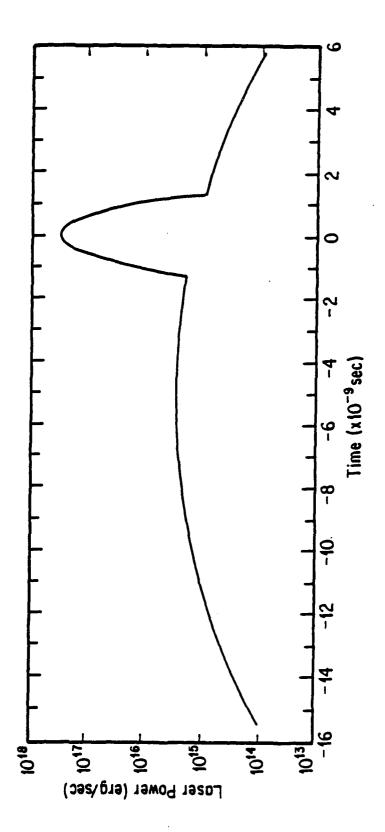


Figure 5: Laser Pulse Shape

with a 5 ns delay between peaks, by a main pulse, 1 ns long and depositing 15J of energy. The long preheating pulse creates a plasma with reduced density gradients, thus enhancing the absorption of the main pulse.

The outcome of the experiment is that most of the energy in the range of interest is emitted in the He-like end H-like q-lines, inasmuch as the continuum is negligible and the higher lines are at least one order of magnitude smaller; the line ratio of He<sub>q</sub> to H<sub>q</sub>, that is, the ratio of the total energies emitted in these two lines, is about 2, and the total efficiency, that is, the ratio of total emitted x-ray energy to total deposited laser energy, is found to be of a couple of percent.

In order to compare our calculations to these results, we must first match our input parameter set to the experimental conditions. Because our code gives power output at each time step, whereas the experiment yields total energy output in a given x-ray line, we must perform at times integration. A simple procedure to do this is to perform a rectangular integration over all the time steps offered by the hydrocode. This being extremely expensive it seemed fit, and well within the precision level of the rest of the approximations, to use only a limited number of representative steps.

The hydrocode being adaptive, the time step is automatically adjusted so that an approximately constant change in thermodynamical properies occurs from step to step. It seems therefore reasonable to choose a constant pace in selecting representative steps, like every

100th or every 300th step. The actual number can be selected by the user to fit best the problem they are treating.

To match the code to the experimental conditions requires some more careful justification. In the first place, our code is designed to model spherical targets, whereas the experiment described above involves flat targets. It has been shown, however, [10] that the hydrodynamics of the expansion of a laser-heated flat target, having a spot diameter D, can be modeled with good accuracy as a conical section of a spherical expanding plasma (see Figure 6).

More precisely, starting with a spherical target with radius R=D and heating it with a spherically symmetric laser, with the same intensity as for the flat target, the portion of the ensuing plasma comprised inside a cone of semiaperture 30° and vertex in the center of the sphere will model very closely the actual plasma generated by the flat target. This model is particularly good near the axis of the cone, whereas it fails at the edge of it, as one would reasonably expect. Of course, the laser energy deposited on the whole model sphere is sixteen times the energy actually deposited on the real flat target, and this must be taken into account in choosing input power parameters for the code.

The absorption routine in the hydrocode considers only inverse bremstrahlung, and actually deposits only some fraction of the total laser energy. To fit Epstein's experiments best, we adjusted the total laser power so that the predicted energy absorption would equal the

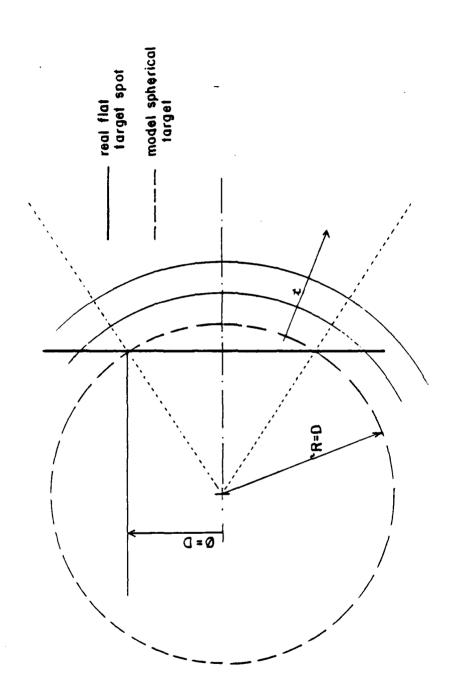
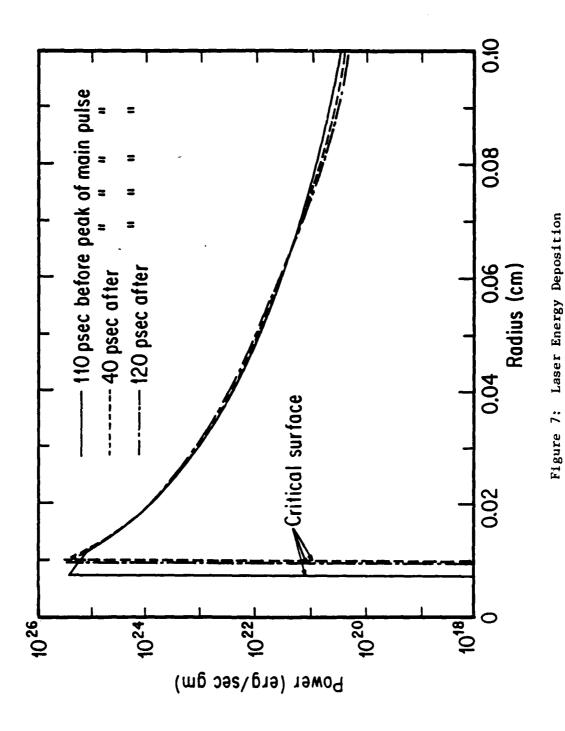


Figure 6: Target Model

what the energy deposition looks like as a function of radius, around the peak of the laser pulse. The cut-off at the critical surface is very evident. Thanks to preheating, a large fraction of the laser energy (58%) gets deposited. Under such conditions neglect of absorptive mechanisms other than IB is believed to be a reasonable approximation.

Table 1 shows the parameters of the run. Figures 8 to 11 show the spatial behaviour of the plasma, as calculated by the hydrodynamics and heat flow code. Figure 8 shows the electronic temperature: it follows somewhat the shape of the laser deposition around the critical surface. Then, proceding outward, one may see that the high electronic thermal conductivity tends to homogenize the temperature.

In Figure 9 we show the ionic temperature. Ions are heated by cross-relaxation with the electrons, and by viscosity when shock waves pass through. As an example of viscous heating, there is, in Figure 9, a second peak at about 0.06 cm radius that clearly cannot be the result of electron heating. This suggests that a shock is building up. This impression is confirmed by a close scrutiny of Figure 10. A small density peak is building up at the same radial position, because of the sudden heating by the short main pulse.



## TABLE 1

Target:

Material

Aluminum

Size

Radius = 40 µm

Initial temperature

0.25 eV

Laser Pulse:

Shape

2 gaussians

Energy

E1 = 2.6 J

E2 = 26.0 J

Full width at

FWHM1 = 10.0 nsec

Half maximum

FWHM2 = 1.0 nsec

Delay between peaks

= 5.0 nsec

Wavelength

= 1.06 μm

Total absorbed

= 16.5 J

energy

(=58%)

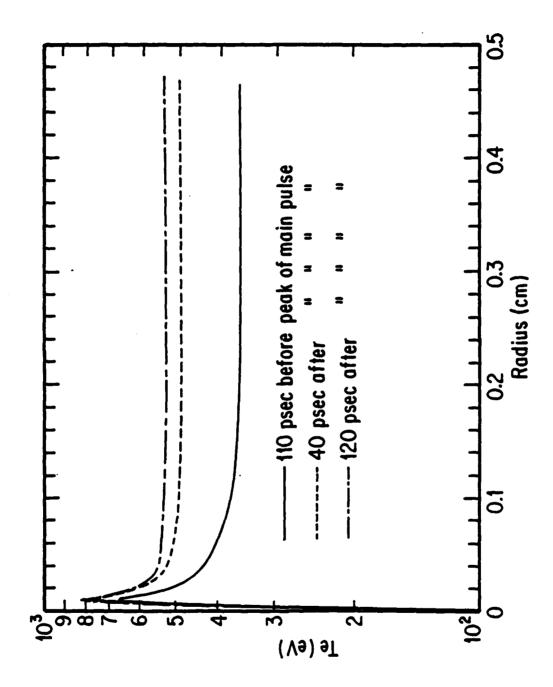
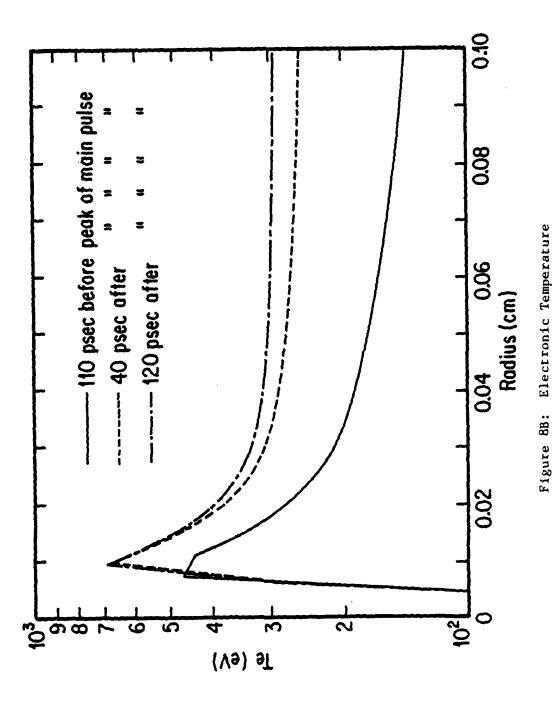
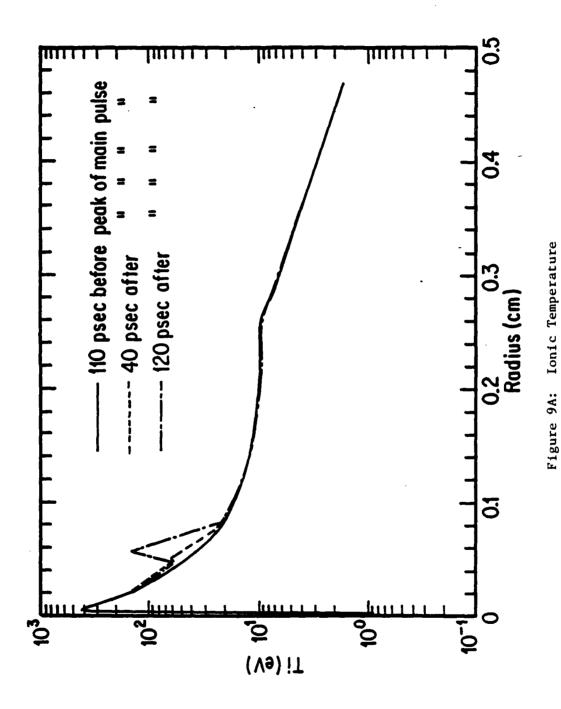
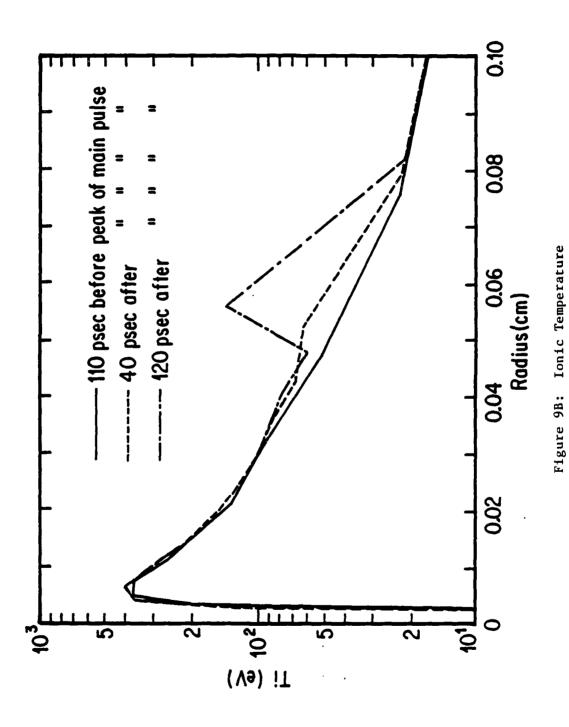


Figure 8A: Electronic Temperature







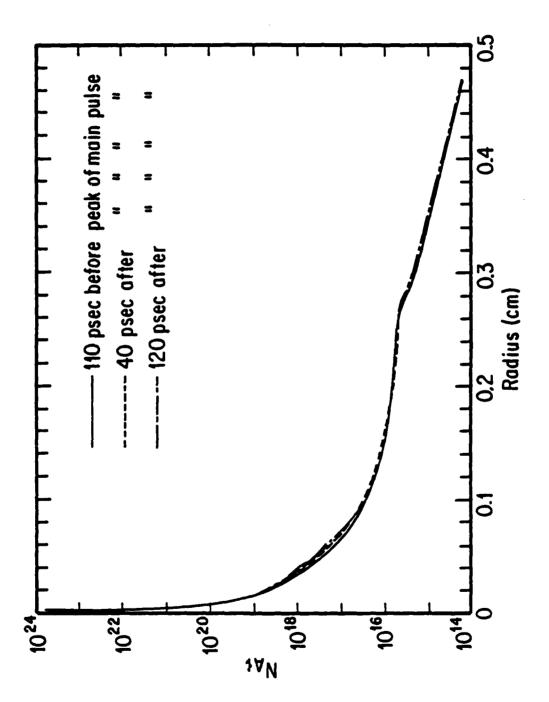
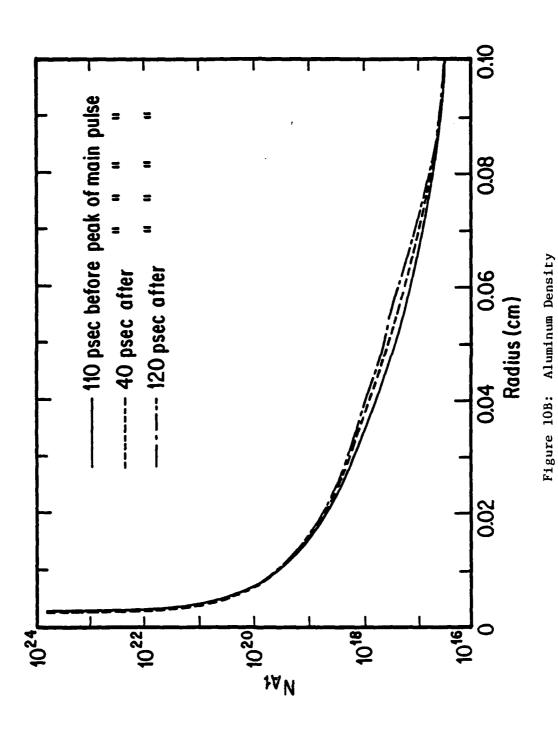


Figure 10A: Aluminum Density



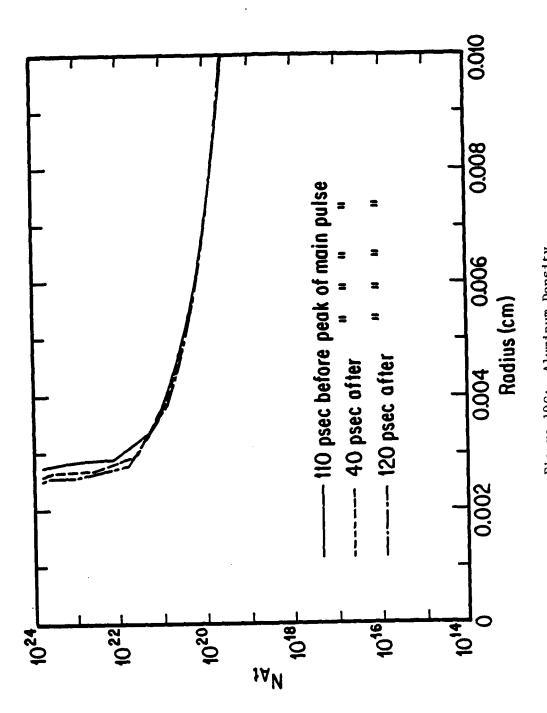
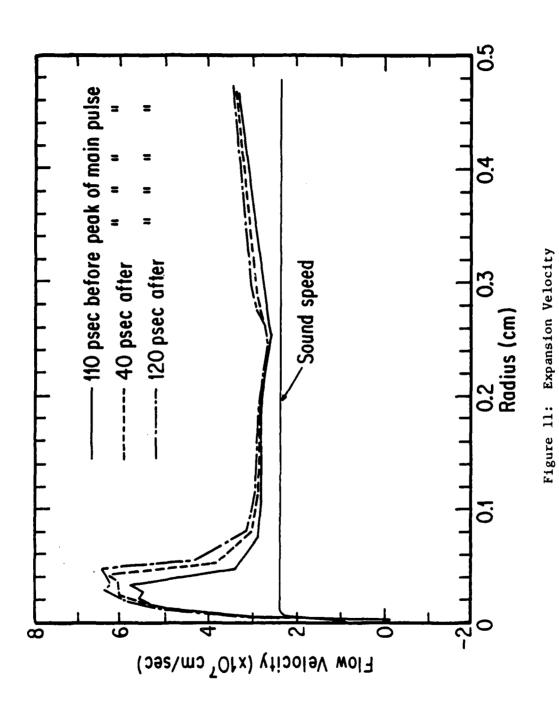


Figure 10C: Aluminum Density



Particularly noteworthy is the expansion velocity (Figure 11) which is above sonic in all that part of the plasma that we may expect to contribute most to the radiation, that is, the part that is dense and hot at the same time. This points to the need for a treatment of the Doppler shift. We can see that this radiating part is a relatively thin shell around the critical surface, since density drops sharply with radius. The effect of the two pulses is very clear. The velocity at large radius is smaller than the velocity close to the critical surface: we must bear in mind that the three curves shown are at three times very close to each other, around the peak of the main pulse. Therefore the effects of this expansion have not reached the more peripheral plasma, whose expansion velocity is still the one due to the preheating pulse.

This graph also supplies evidence for the explanation of the second ionic temperature peak: following the velocity profile inward, the velocity suddenly steepens around r=0.06 cm. A faster expanding plasma is pushing against a slower one, and a shock wave is to be expected.

Figure 12 are the first results of the post-processor. As mentioned earlier, the code recognizes 'cold' zones, and totally neglects them. Therefore no electronic or ionic densities are calculated for such zones. That is why, in Figures 12, such densities start abruptly with a very high value near the critical surface. We will return to these graphs later.

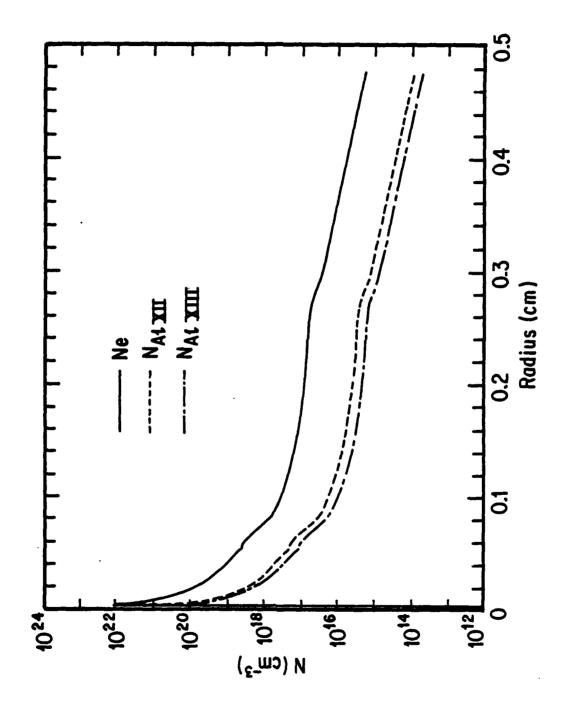


Figure 12A: Electronic and Ionic Densities

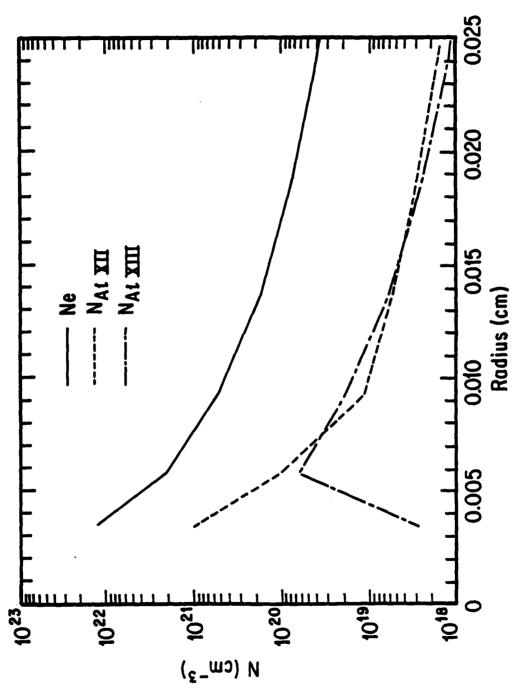


Figure 12B: Electronic and Ionic Densities

In the present calculation we have used 100 photon energy groups per line, 200 for the doublet. Although to predict the total energy output fewer groups would suffice, we found that a much smaller number of them would give a very rough definition to the line profiles.

the code checks itself for consistency, comparing the net collisional pumping power in every zone with the net flux of radiation out of the zone.

As it turns out, the radiation output is perfectly consistent with the collisional power, zone by zone and globally. It is, in fact, a necessary condition, given this physical situation, that net radiation output and net pumping power, for every zone, be equal to each other.

On the other hand, if we look at the laser energy deposition (Figure 7), we notice that almost all the energy is deposited in a region comprising only a couple of zones. This seems to be at the very lowest boundary of acceptable resolution, even taking into account the fact that the various zones, passing through this 'deposition region' as time passes, 'average' in some sense the state of the region. It is necessary to have a finer grid, so that the deposition is smeared through a large number of zones, and we plan on doing so in the very near future.

Figure 15 shows the emitted spectrum, integrated over time. An integration over photon energy shows that  ${\rm He}_a$  and  ${\rm H}_a$  lines account for more than 90% of the total emitted energy, the line ratio of  ${\rm He}_a$  to  ${\rm H}_a$  is 2.5-3.00 and the total efficiency is 4.5-5%: the uncertainty in

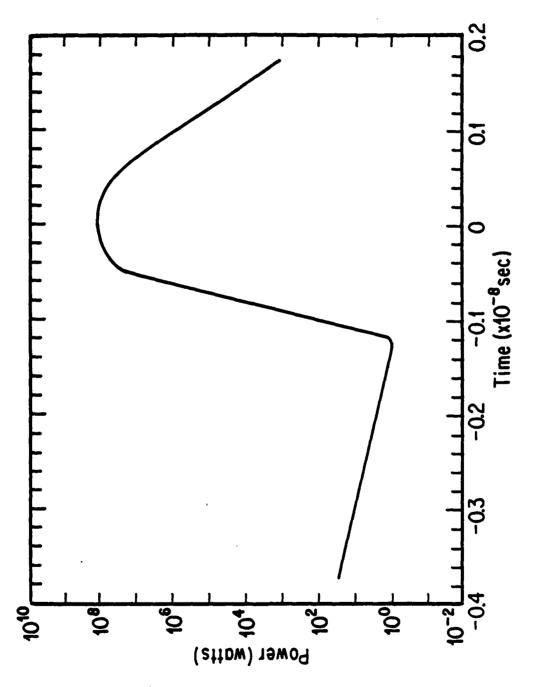


Figure 13: Total Output Power

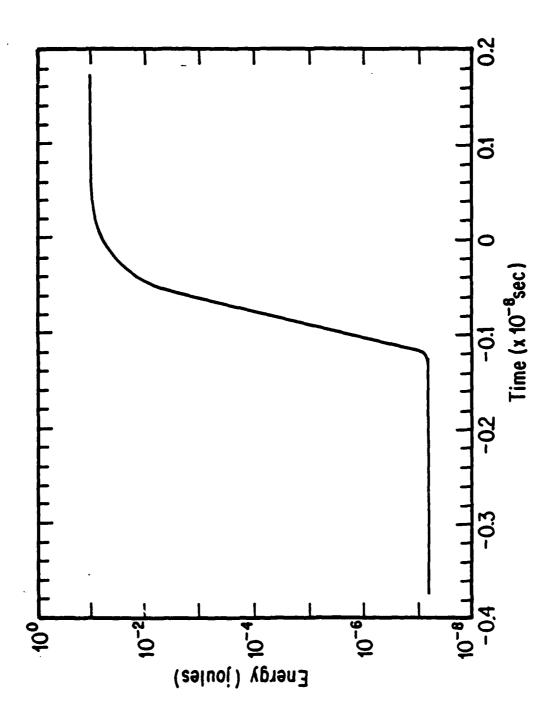


Figure 14: Total Output Energy

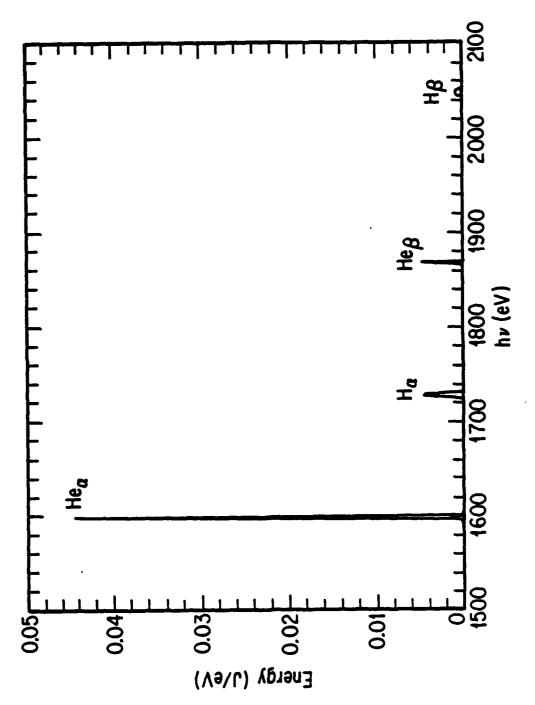


Figure 15: Time-integrated Emission Spectrum

those figures stems from the fact that those quantities are rather sensitive to the exact amount of energy deposited by the laser, and the absolute value of this deposited energy is not easy to measure in experiments. Those results are in good agreement with Epstein's experiments, especially the line ratio, which is a very sensitive measure. Details of the time integrated line shapes are given in Figure 16 to 18.

Figures 19 to 24 are in the same vein, but referring to the instantaneous emission at peak power. The narrow shape of He-like lines (compared to H-like, that is) is explained with the help of Figure 12B. As we see, He-like ion density is very peaked, and rolls off very quickly. H-like ion density, on the contrary, increases at first with radius, and then rolls off more gently. We can hence expect that the He-like emitting zone would be deeper inside the plasma and extend over a smaller thickness of plasma than the H-like. The average flow velocity of the He-like emitting plasma is therefore man-dly smaller than the average flow velocity of the H-like emitting one, this naturally implies a smaller Doppler shift and hence less smearing of the line shape.

To understand the result of the multi-level calculation of the Ha doublet, we have to look at Figures 25. Those line shapes have been obtained by arbitrarily reducing the expansion velocity of the plasma (to 0, 25%, 50% and 75% respectively), and therefore the amount of

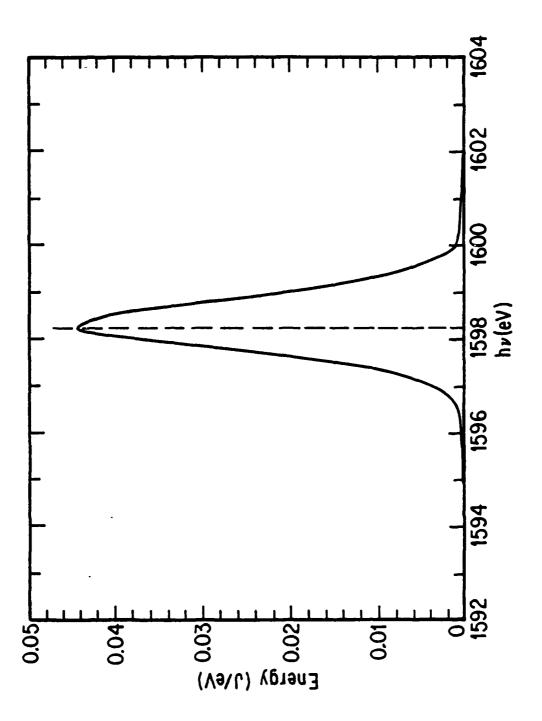


Figure 16: Time-integrated  ${\rm He}_{\alpha}$  Line

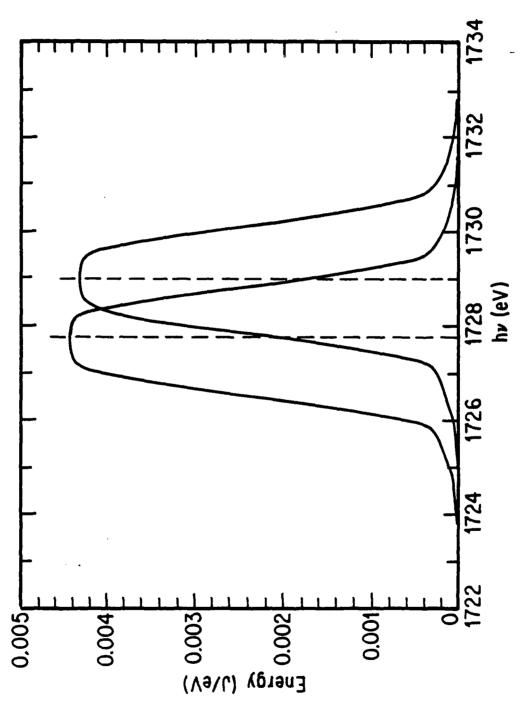


Figure 17A: Time-integrated H Doublet Two-Level Approximation

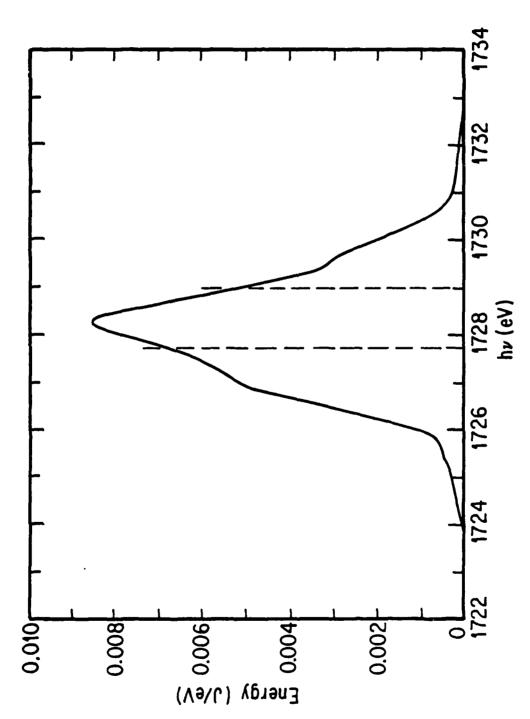


Figure 178: Time-integrated H Doublet

Multi-level Treatment

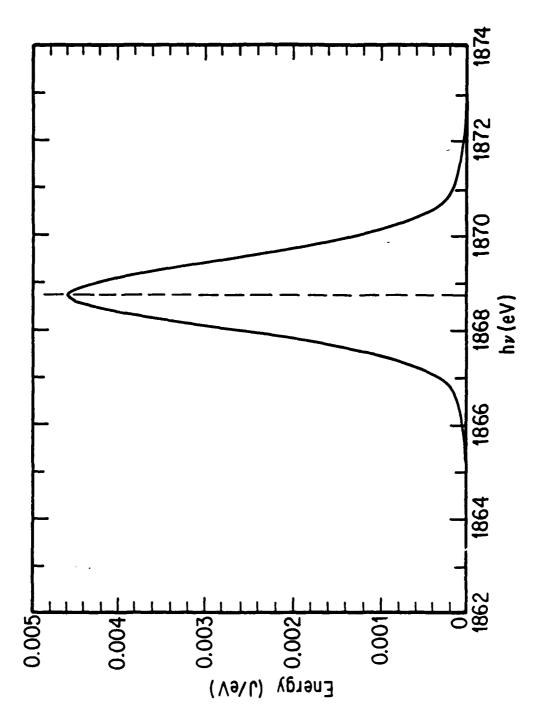
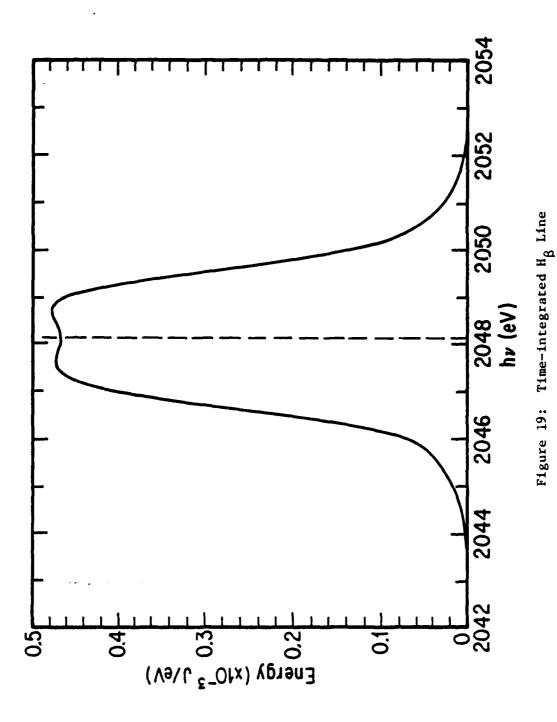
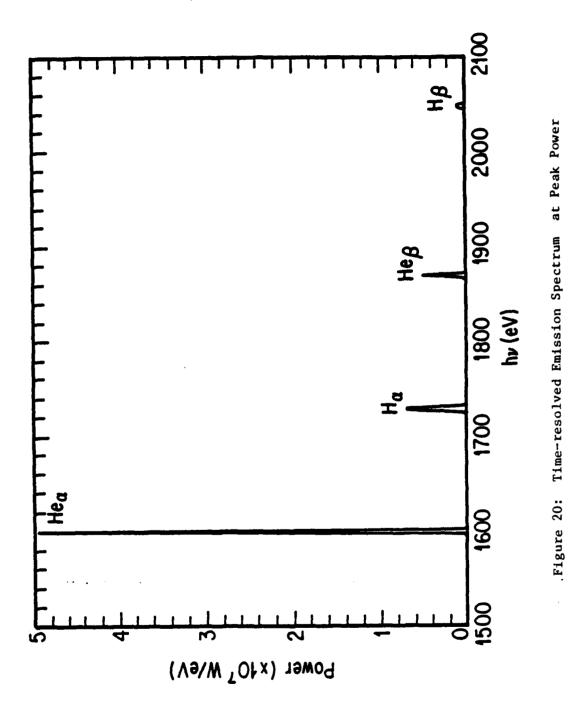


Figure 18: Time-integrated  $He_{eta}$  Line





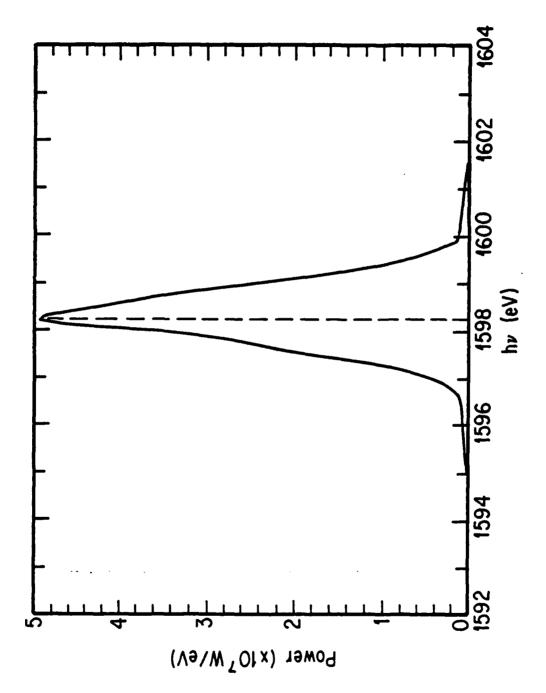


Figure 21: Time-resolved  $He_{\alpha}$  at Peak Power

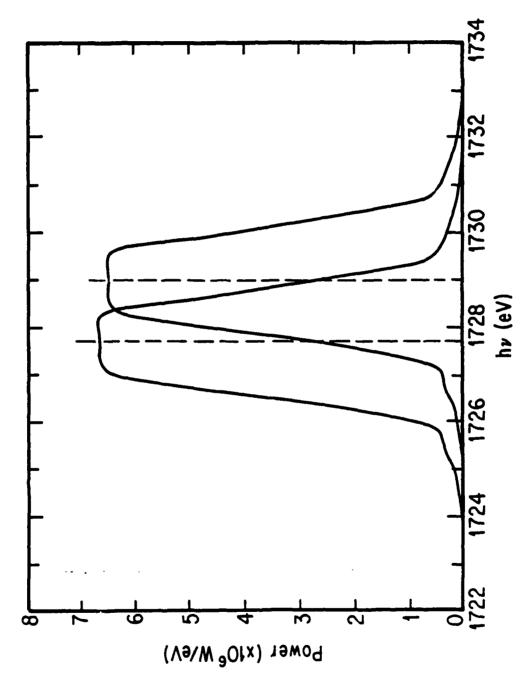
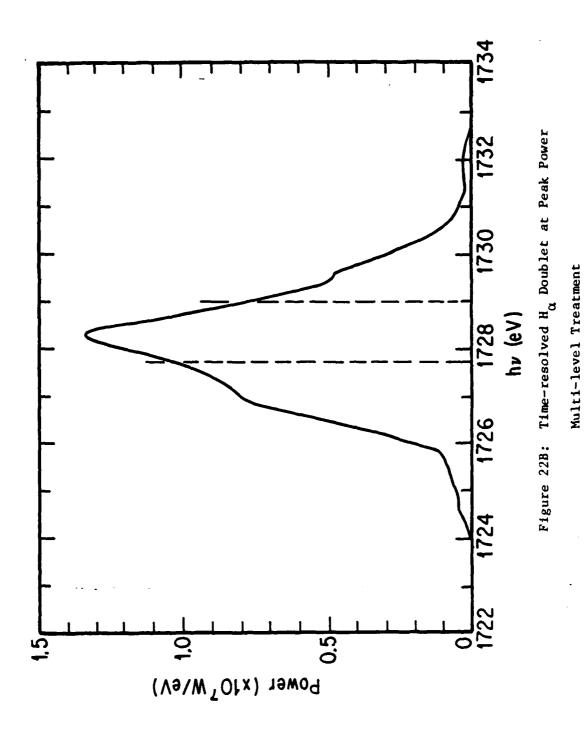


Figure 22A: Time-resolved H Doublet at Peak Power

Two Level Approximation



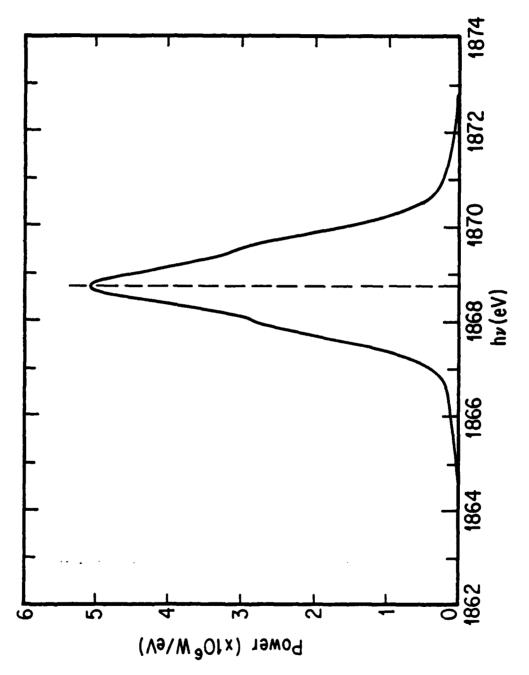
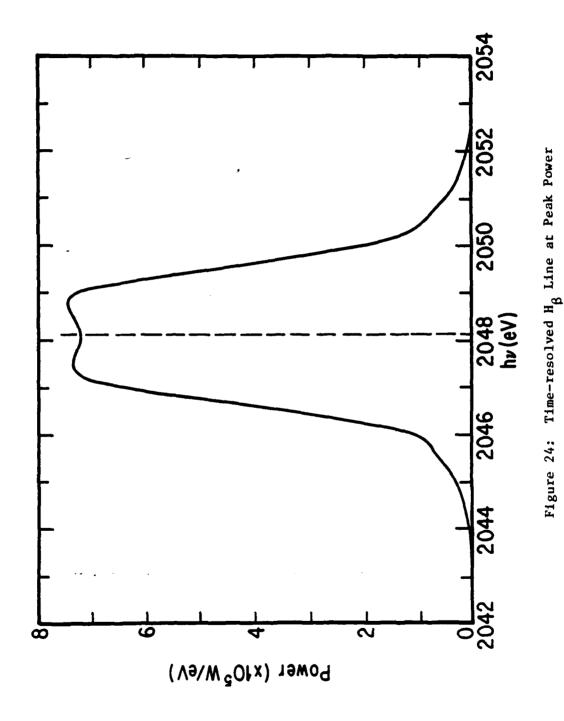
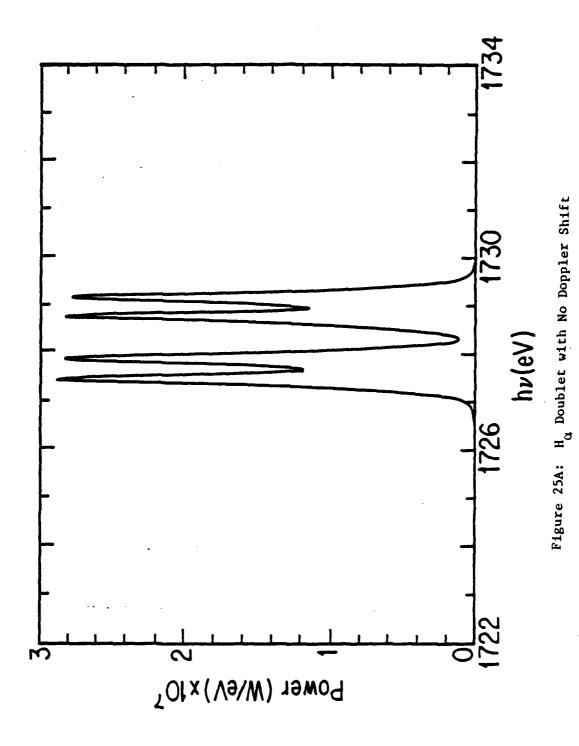
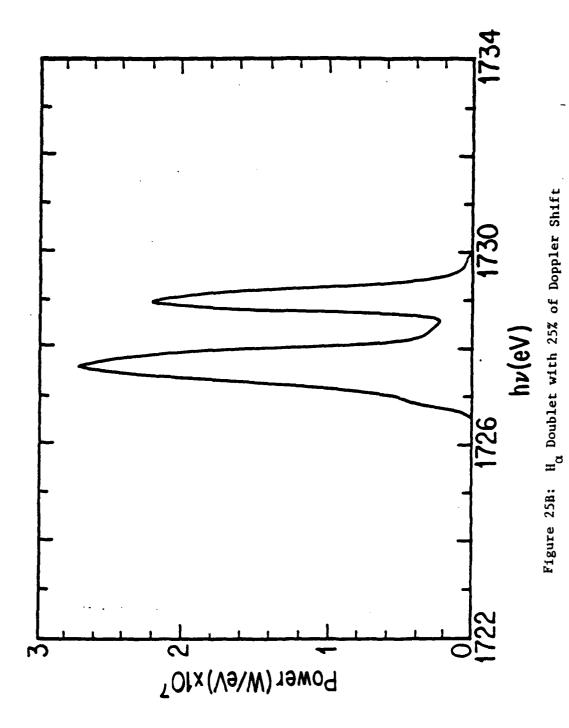
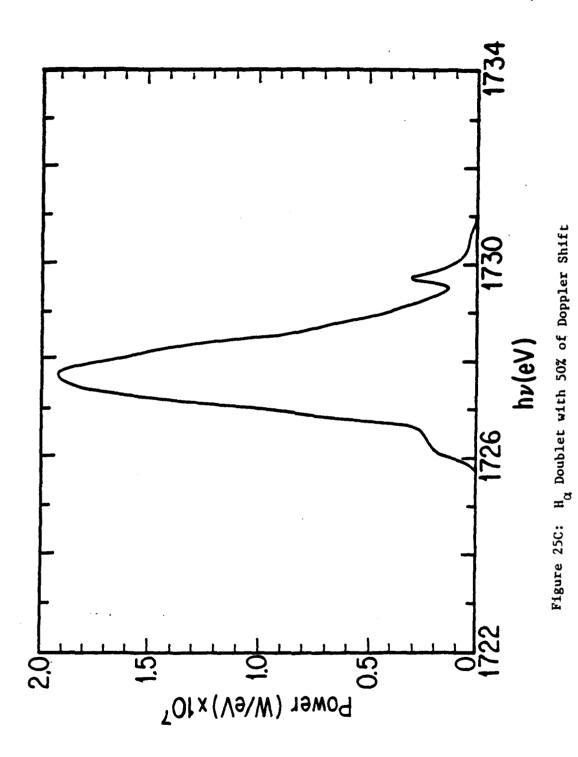


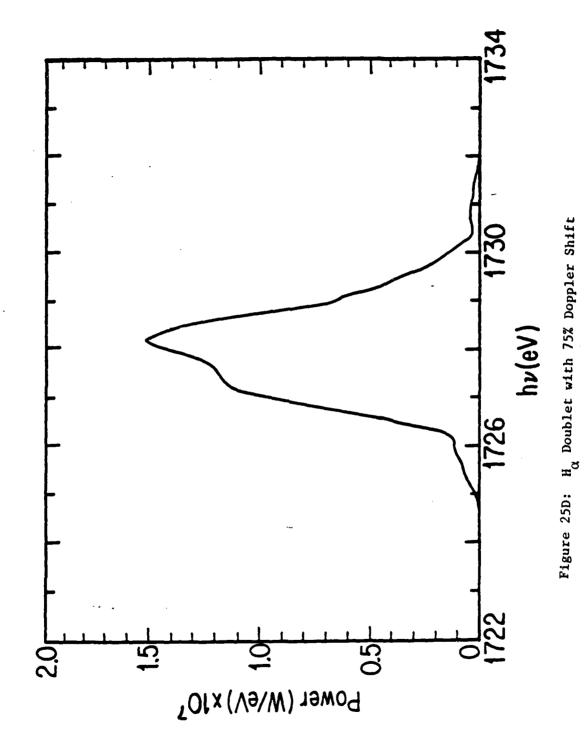
Figure 23: Time-resolved Heg Line at Peak Power











Doppler shift. As shift increases the second line of the doublet gives up its energy to the first line.

This can be explained as follows: light emitted in the second line at some point in the plasma is reabsorbed in the first line at points further out, therefore contributing to enhance the first line's excited level population, whereas light coming from inside cannot excite the second line at outer points. The global effect of this phenomenon is to shift radiation from the second to the first line in the doublet. This is more markedly so the larger the Doppler shift, until, if the plasma is expanding fast enough, the second line completely disappears.

Of course, the opposite is true for light transported inward, so that we can think of the population of the excited levels of the two lines, when the two lines are treated together, as 'tilted' toward the second line in the inner plasma and toward the first line in the outer plasma, as compared to the populations we would find treating one line at a time.

### CHAPTER 6

### CONCLUSIONS

A code has been developed that is both economical and accurate. It is designed so that more accuracy can be obtained, of course with a higher cost, or it can be made more economical, whenever less accuracy is needed. The results are in good agreement with the experimental work to the extent of the experimental resolution. Unfortunately experiments are as yet unable to resolve line shapes. The detail with which the line shapes can be predicted by our code have already prompted experimentalists to try and improve the resolution of their experiments to measure line shapes.

Whenever experimental data on line shapes will be available, we will check our results against it. We plan also on using our model to predict diagnostics.

### APPENDIX A

### VARIOUS DERIVATIONS

## a) The Rate Equation

From (II-1), with the condition 
$$\frac{dn_2}{dt} = 0$$

(steady state assumption), we obtain

$$(\Omega_{12}n_e + B_{12}) \int_0^\infty \phi_E J_E dE n_1 = (A_{12} + \Omega_{12}n_e + B_{12}) \int_0^\infty \phi_E J_E dE n_2$$

with the relations [9]

$$\Omega_{21} = \Omega_{12} - \frac{g_1}{g_2} \exp \left\{ -\frac{E_{21}}{KT_e} \right\}$$

$$B_{12} = \frac{g_2}{-----} B_{21}$$
 ( $g_1$  and  $g_2$  are the statistical weights of levels 1 and 2)

$$B_{21} = \frac{h^3c^2}{2} \frac{A_{21}}{(E_{21})^3}$$

Therefore we can write a system of 2 equations in n1, n2:

$$\frac{\Omega_{12}n_{e} + \frac{g_{2}}{g_{1}}}{n_{1}} = \frac{B_{21} \int_{E}^{\Phi} E^{J} E^{dE}}{E_{21}}$$

$$\frac{E_{21}}{KTe} + B_{21} \int_{E}^{\Phi} E^{J} E^{dE}$$

$$\frac{A_{21} + \Omega_{12}n_{e}}{g_{2}} = \frac{g_{1}}{g_{2}} + B_{21} \int_{E}^{\Phi} E^{J} E^{dE}$$

$$n_1 + n_2 = N_i$$

which yields n<sub>1</sub> and n<sub>2</sub>.

Al so

$$\int_{\Phi_{E}} \int_{E^{dE}} = \sum_{m \in \Phi^{m} J^{m} \Delta E^{m}}$$

where the sum is over photon energy groups

# b) The Finite Difference Equation

We will use the following notations:

$$R1_k = r_{k-1}, R2_k = r_k$$

 $A1_k$ ,  $A2_k$  and  $V_k$ , area of the inner and outer surfaces and

volume of the shell.

The subscript 'in' refers to the surface through which the ray enters the zone, 'out' to the other surface.

The energy flux  $F_R(r)$  is defined as

$$\vec{F}_{E}(\vec{r}) = \int_{A\Omega} \vec{a} I_{E}(\vec{r}, \vec{a}) d\vec{a}$$

Simple energy-conservation considerations yield

$$\nabla \cdot \dot{F}_{E} = \frac{\text{Source}}{\text{Unit Volume}} =$$

$$A_{21}n_{2}$$
  $E_{21}$   $\phi_{E}$  -  $(B_{12}n_{1}-B_{21}n_{2})$   $E_{21}$   $\phi_{E}$   $J_{E}$ 

where

A<sub>12</sub>, B<sub>12</sub>, B<sub>12</sub> = Einstein coefficients

φ E = Absorbtion profile = Emission profile

$$J_{E}(\vec{r}) = \frac{\int_{\Delta\Omega} I_{E}(\vec{r}, \vec{Q}) d\vec{Q}}{\int_{\Delta\Omega} d\vec{Q}}$$

Let us consider a spherical shell, with constant thermodynamical properties, bounded by two spherical surfaces of radii R1 and R2.

The net flux of  $\overrightarrow{F}_{E}(x)$  out of the shell is

$$\oint_{E} \vec{F}_{E}(\vec{r}) \cdot \vec{n} dA$$

$$= \int_{S2} \vec{F}(R2) \cdot \hat{r} dA - \int_{S1} \vec{F}(R1) \cdot \hat{r} dA$$

$$= 2\pi A2 \int_{E} \mu_{2} I_{E}(R2, \mu_{2}) d\mu_{2} - 2\pi A1 \int_{E} \mu_{1} I_{E}(R1, \mu_{1}) d\mu_{1}$$

where  $\mu = \mu(r)$ ,  $\mu_1 = \mu(R1)$ ,  $\mu_2 = \mu(R2)$ .

On the other hand

$$\nabla \cdot \overrightarrow{F}_{E} = A_{21} n_{2} E_{21} \phi E \frac{2\pi \int d\mu}{4\pi}$$

$$- (B_{12}\mu_1 - B_{21}\mu_2)E_{21} \phi_E - \frac{2\pi \int I_E(r,\mu)d\mu}{4\pi}$$

Now:

$$\oint_{S} \vec{F}_{E} \cdot \vec{n} dA = \int_{V} \nabla \cdot \vec{F}_{E} dV$$

$$2\pi \text{ A2} \int \mu_{2} \text{ I}_{E}(R2, \mu_{2}) d\mu_{3} - 2\pi \text{ A1} \int \mu_{1} \text{ I}_{E}(R1, \mu_{1}) d\mu_{1} =$$

$$\iiint \left( \frac{A_{2} \ln_{2} E_{3}}{4\pi} \phi_{E} - \frac{(B_{1} 2 \ln_{1} - B_{2} \ln_{2})}{4\pi} E_{2} + \phi_{E} \text{ I}_{E}(r, \mu) \right) d\mu d\mu_{1} =$$

$$= 2\pi \iiint \left\{ \iint \left( S \phi_{E} - H \phi_{E} \text{ I}_{E}(r, \mu) \right) d\mu d\mu_{1} \right\} dV$$

where

$$S = \frac{A_{21}n_2E_{21}}{4\pi} ,$$

$$H = \frac{B_{12}n_1 - B_{21}n_2}{A\pi} E_{21}$$

This yields the finite differences equation.

A2 
$$\mu_{2}$$
,  $\ell$   $\Delta \mu_{2}$ ,  $\ell$   $I_{2}$  - A1  $\mu_{1}$ ,  $\ell$   $\Delta \mu_{1}$ ,  $\ell$   $I_{1}$ ,  $\ell$ 

=  $V \phi_{E} \left( S \widetilde{\Delta \mu}_{\ell} - H \widetilde{\Delta \mu}_{\ell} \widetilde{I}_{\ell} \right)$ 

where S and H are constants and  $\widetilde{\Delta\mu}_{L}$ ,  $\widetilde{I}_{\underline{E}}$  are properly defined averages through the volume.

Finally:

A2 
$$\mu_{2,\ell}$$
  $\Delta\mu_{2,\ell}$   $I_{2,\ell}^{m}$  - A1  $\mu_{1,\ell}$   $\Delta\mu_{1,\ell}$   $I_{1,\ell}^{m}$  =  $V \varphi^{m}$  (S-H  $\widetilde{I}_{\ell}^{m}$  )  $\widetilde{\Delta\mu}\ell$ 

Two cases are possible:

- 1) Forward, that is  $\mu_1$  and  $\mu_2>0$  Then  $I_1$   $\chi$  is specified as boundary condition
- 2) Backward, that is  $\mu_1$  and  $\mu_2<0$  here the boundary condition is on  $I_{2,\,\ell}$  Accordingly, we have the following two equations:

1) 
$$I_{2,\ell}^{m} = \frac{A1\mu_{1,\ell}\Delta\mu_{1,\ell}}{A2\mu_{2,\ell}\Delta\mu_{2,\ell}}$$
  $I_{1,\ell}^{m} + \frac{V\phi^{m}\widetilde{\Delta\mu}\ell}{A2\mu_{2,\ell}\Delta\mu_{2,\ell}}$  (S-H  $\widetilde{I}_{\ell}^{m}$ )

2) 
$$I_{1,2}^{m} = \frac{A2\mu_{2,\ell}\Delta\mu_{2,\ell}}{A1\mu_{1,\ell}\Delta\mu_{1,\ell}}$$
  $I_{2,\ell}^{m} + \frac{V\phi^{m}\widetilde{\Delta\mu_{\ell}}}{A1\mu_{1,\ell}\Delta\mu_{1,\ell}}$  (S-H  $\widetilde{I}_{\ell}^{m}$ )

# (a') In the Critical Zone

For the limiting case of the critical zone, notice that

$$\mu_{\chi}$$
, =  $-\mu_{\chi}$ ,  $\Delta\mu_{\chi}$ , =  $\Delta\mu_{\chi}$ .

the formula used is

$$I_{2,\ell}^{m} = I_{2,\ell}^{m} + \frac{V \phi^{m} \Delta \mu}{A 2 \mu_{2,\ell} \Delta \mu_{2,\ell}}$$
 2S -  $H(I_{\ell}^{m} + I_{\ell}^{m})$ 

b'') In A Cold Zone

If 
$$S = H = 0$$
, then  $I_{\ell}^{m}(r) = I_{in,\ell}^{m} - \frac{R_{in}^{2}}{r^{2}}$ 

therefore:

$$I_{\ell}^{m} = I_{in, \dot{\ell}}^{m} \frac{A_{in}\Delta R}{V}$$

$$I_{\text{out},\ell}^{m} = I_{\text{in},\ell}^{m} \frac{R_{\text{in}}^{2}}{R_{\text{out}}^{2}}$$

# c) Averaging of $\phi_E$ Through Zone

$$\phi_{E} = \frac{1}{\sqrt{\pi} \Delta E_{O}} \exp \left\{ -\left[ \frac{E(1 - \frac{v\mu}{c}) - E_{O}}{\Delta E_{O}} \right]^{2} \right\}$$

$$V\mu = \left[ \frac{v\mu}{c} \right]_{1} + \frac{\left[ \frac{v\mu}{c} \right]_{2} - \left[ \frac{v\mu}{c} \right]_{1}}{\Delta r} (r - r_{1})$$

$$\phi_{E} = \frac{1}{\sqrt{\pi} \Delta E_{O}} \exp \left\{ -\left[ \frac{E - E_{O}}{\Delta E_{O}} - \frac{E}{\Delta E_{O}} \left( \left[ \frac{v\mu}{c} \right]_{1} + \frac{v\mu}{c} \right] \right] + \frac{\left[ \frac{v\mu}{c} \right]_{2} - \left[ \frac{v\mu}{c} \right]_{1}}{\Delta r} \right\}$$

Set:

$$A = \frac{E - E_o}{\Delta E_o} - \frac{E}{\Delta E_o} \begin{bmatrix} \frac{\nabla \mu}{c} \end{bmatrix}_1$$

$$B = -\frac{E}{\Delta E_{o}} \left( \begin{bmatrix} -v\mu \\ c \end{bmatrix}_{2} - \begin{bmatrix} -v\mu \\ c \end{bmatrix}_{1} \right) \frac{1}{\Delta r}$$

So:

$$\phi_{E} = \frac{1}{\sqrt{\pi}\Delta E_{o}} - \exp\left\{-\left[A + B(r-r_{1})\right]^{2}\right\}$$

$$\int_{E}^{r_{2}} \frac{\int_{E}^{r_{2}} dr}{r_{1}} = \frac{1}{2\Delta E_{o}\Delta r} - \frac{1}{\sqrt{\pi}} \int_{r_{1}}^{r_{2}} e^{-\left[(A + B(r-r_{1}))\right]} dr = \frac{1}{2\Delta E_{o}\Delta r} - \frac{1}{B} - \frac{2}{\sqrt{\pi}} \int_{r_{1}}^{r_{2}} - \left[A + B(r-r_{1})\right]^{2} d\left[A + B(r-r_{1})\right]$$

$$= \frac{1}{2\Delta E_{o}\Delta r} - \frac{1}{B} - \frac{2}{\sqrt{\pi}} \int_{e}^{A + B\Delta r} - \frac{1}{e^{-y^{2}}} dy$$

$$= \frac{1}{2\Delta E_{o}B\Delta r} \left[ \frac{2}{\sqrt{\pi}} \int_{0}^{A + B\Delta r} - \frac{2}{\sqrt{\pi}} \int_{0}^{A - y^{2}} dy \right] = \frac{1}{2\Delta E_{o}B\Delta r} \left[ erf(A + B\Delta r) - erf(A) \right]$$

$$A = \frac{E\left[1 - \frac{v\mu}{c}\right] - E_{o}}{\Delta E_{o}}$$

$$A+B\Delta r = \frac{E\left[1-\frac{\forall \mu}{c}\right]^{2}-E_{o}}{\Delta E_{o}}$$

$$B\Delta E_{o}\Delta r = -E\left\{ \left[ 1 - \frac{\nabla \mu}{c} \right]_{2} - \left[ 1 - \frac{\nabla \mu}{c} \right]_{2} \right\}$$

$$\frac{1}{2E} = \frac{1}{\frac{1-\frac{\nu\mu}{c}}{\Delta E_{o}}} - erf \left\{ \frac{E\left[1-\frac{\nu\mu}{c}\right]_{2}-E_{o}}{\Delta E_{o}} \right\}$$

### APPENDIX B

### CONTRIBUTION OF THE CONTINUUM

# a) Continuum emission and absorption

# 1) Absorption

$$K_{E}^{cont} = K_{E}^{ff} + K_{E}^{bf}$$

$$K_{E}^{ff} = C_{k}^{ff} \left[ \frac{n_{e}}{E} \right]^{3} \frac{1}{\sqrt{T_{e} N_{e}}}$$

$$C_{k}^{ff} = 2.4234 \ 10^{-37}$$

$$K_E^{bf} = C_k^{bf} - \frac{N}{E^3} \sum_{i} \left\{ \frac{(i-1)^4}{N_i} \sum_{j} \frac{n_{i,j}}{(q_{i,j})^5} \right\}$$

$$C_k^{bf} = 1.9924 \ 10^{-14}$$

If we assume  $n_{i,G.S.} = N_i$ ,  $n_{i,j} \approx 0 \ \forall j \neq G.S.$  then the above equation simplifies to

$$K_E^{bf} = C_k^{bf} \frac{N}{-E^3} \sum_{i=\frac{(i-1)^4}{(q_{i,g.s.})^5}}$$

Since we are considering an interval around  $\boldsymbol{E}_{i,j}$ , we make the further simplification that

$$\frac{1}{E^3} - \frac{1}{E_{i,j}^3}$$

in both formulas for KEff and KEbf.

## 2) Emission

sgcont =sgff +sgfb

$$s_{\rm E}^{\rm ff} = c_{\rm E}^{\rm ff} \sqrt{T_{\rm e}} \quad n_{\rm e} \left\{ \sum_{i (i-1)^2 n_i} \right\} \frac{e^{-E/T_{\rm e}}}{T_{\rm e}}$$

$$c_{\rm E} = 9.5842 \quad 10^{-14}$$

$$\varepsilon_{E}^{fb} = C_{E}^{fb} n_{e} T_{e} \left[ \sum_{i} \left\{ (i-1)N_{i} \left( \frac{U_{i}}{T_{e}} \right)^{3/2} \right\} \right] \exp \left\{ -\frac{\Delta U_{i}}{T_{e}} \right\} .$$

$$\sum_{j} \left(1 - \frac{n_{i,j}}{N_{i}}\right) \xrightarrow{\exp\left\{-\frac{U_{i} - E_{i,j}}{T_{e}}\right\}} \left\{ \int_{-E/T_{e}}^{-E/T_{e}}$$

$$c_E^{fb} = 5.1965 \cdot 10^{-14}$$

Again, assuming  $n_{i,g,S} = N_i$ ,  $n_{i,j} = 0$   $\forall j \neq G.S.$ , and neglecting the correction for the lowering of the continuum  $(\exp[-\frac{\Delta U_i}{Te}] = 1)$ :

$$s_{E}^{fb} = C_{E}^{fb} n_{e} T_{e} \left[ \sum_{i} \left\{ (i-1) N_{i} \left( \frac{U_{i}}{T_{e}} \right) \right\} \right]$$

$$\sum_{j} \frac{exp\left\{-\frac{U_{i}-E_{i,j}}{T_{e}}\right\}}{(q_{i,j})^{3}}$$

The results show an energy emitted in the continuum per unit eV that is much smaller than the one in the line.

Extrapolating the result to the entire range 1500 - 2500 eV gives a total energy emitted in the continuum in such interval \*\* about 100 times smaller than the energy emitted in the lines.

$$E_{cont} \simeq 9.5 \ 10^{-7} \ \text{J/eV} \Rightarrow \sim 9.5 \ 10^{-4} \ \text{J}$$

from hv = 1500 to hv = 2500.

 $E_{1ine} \simeq 9.5 \ 10^{-2} \ from \ h^{\lor} = 1500 \ to \ h^{\lor} = 2500.$ 

<sup>\*\*</sup> For the examples we treated.

### REFERENCES

- 1. Holstein, D. T. "Imprisonment of Resonance Radiation in Gases," <a href="https://example.com/Physical Review">Physical Review</a>, 72, pp. 1212-1233, 1947.
  - Holstein, D. T., "Imprisonment of Resonance Radiation in Gases," <a href="https://example.com/Physical Review">Physical Review</a>, 83, pp. 1159-1168, 1951.
- 2. McWhirter, R. W. P. "Spectral Intensities," in <u>Plasma Diagnostic Techniques</u>, edited by R. H. Huddlestone and S. L. Leonard, pp. 201-264, 1968.
- 3. Colombant, D. G., "Laser Target Model," Physics of Fluids, 18, pp. 1687-1697, 1975.
- 4. Summers H. P., 'The Ionization Equilibrium of H-like to Ar-like Ions of Elements," Monthly Notice of the Royal Astronomical Society, 169, pp. 663-680, 1974, and Appleton Laboratory IM367, University of Cambridge, U. K., 1974.
- 5. Matzen, M. K., 'Impact of Nonequilibrium Ionization and Recombination Processes on the Evaluation of Laser-Produced Plasmas," Physics of Fluids, 22, pp. 449-453, 1979.
- 6. Landshoff, R. K. and J. D. Perez, "Determination of Plasma Parameters of Laser-Produced Aluminum Plasma from X-ray Line Radiation," <a href="Physical Review">Physical Review</a>, 13, pp. 1619-1632, 1976.
- 7. Epstein, H. M., et al., "Laser Plasma X-ray Source Optimization for Lithography," SPIE, 385, pp. 141-145, 1983.
- 8. McLean, E. A., et al., "Observation of Magnetic Fields in Laser-Produced Plasma Using the Zeeman Effect," Physics of Fluids, 27, pp. 1327-1335, 1984.
- 9. Mihalas, D., "Stellar Atmospheres," II Edition, W. H. Freeman and Co., 1978.
- 10. Morse, R. L. and R. L. McCrory, Unpublished.